



Cite this: *Mater. Adv.*, 2021,  
2, 1676

# Preparation and characterization of sodium-ion conductive Na<sub>3</sub>BS<sub>3</sub> glass and glass–ceramic electrolytes†

Fumika Tsuji,<sup>a</sup> Akira Nasu,<sup>a</sup> Chie Hotehama,<sup>a</sup> Atsushi Sakuda,<sup>id</sup><sup>a</sup>  
Masahiro Tatsumisago<sup>a</sup> and Akitoshi Hayashi<sup>id</sup>★<sup>ab</sup>

In order to find suitable solid electrolytes for all-solid-state sodium batteries, sulfide electrolytes composed of tetrahedral structural units such as PS<sub>4</sub>, SnS<sub>4</sub> and SbS<sub>4</sub> have been widely studied. In this paper, the ionic conductivities of Na<sub>3</sub>BS<sub>3</sub> *ortho*-thioborate electrolytes with triangular BS<sub>3</sub> units are firstly reported. Na<sub>3</sub>BS<sub>3</sub> glass was prepared *via* a mechanochemical process from crystalline Na<sub>3</sub>BS<sub>3</sub> (monoclinic phase). The crystalline Na<sub>3</sub>BS<sub>3</sub> was pre-synthesized from a mixture of Na<sub>2</sub>S, B, and S due to the instability of the B<sub>2</sub>S<sub>3</sub> compound. A new metastable phase of trigonal Na<sub>3</sub>BS<sub>3</sub> was precipitated as the primary phase by crystallization of the Na<sub>3</sub>BS<sub>3</sub> glass. The prepared glass–ceramic electrolyte showed a higher ionic conductivity than the monoclinic Na<sub>3</sub>BS<sub>3</sub> phase. The Na<sub>3</sub>BS<sub>3</sub> glass showed the highest conductivity of  $1.1 \times 10^{-5} \text{ S cm}^{-1}$ , which was higher than that of conventional Na<sub>3</sub>PS<sub>4</sub> glass. Furthermore, the Na<sub>3</sub>BS<sub>3</sub> glass showed a superior formability and electrochemical stability to Na<sub>15</sub>Sn<sub>4</sub> negative electrode. An all-solid-state cell with the Na<sub>3</sub>BS<sub>3</sub> glass as an electrolyte successfully operated as a secondary battery at 60 °C. It is concluded that the Na<sub>3</sub>BS<sub>3</sub> glass with triangular structural units has appropriate properties as a solid electrolyte for application to all-solid-state sodium batteries. The results of this study extend research on multi-component sulfide electrolytes with triangular BS<sub>3</sub> structural units and contribute to the development of solid electrolytes for all-solid-state batteries.

Received 9th October 2020,  
Accepted 31st January 2021

DOI: 10.1039/d0ma00777c

rsc.li/materials-advances

## 1. Introduction

Sodium-ion batteries with their associated low costs and abundant sodium reserves have attracted significant attention as promising next-generation large-scale energy storage systems to replace lithium-ion batteries. Because sodium has a similar electrochemical performance to lithium, such as standard reduction potential, sodium batteries have the potential to exhibit a high performance.<sup>1–3</sup> As one example of sodium-ion batteries, sodium–sulfur batteries can function as a stationary storage system. However, they require a high temperature of over 300 °C to operate with their molten electrodes, which causes cost and safety concerns.<sup>4</sup> To overcome these issues, all-solid-state sodium–sulfur batteries operated at room temperature are desirable. This requires superior solid electrolytes with high ionic conductivities at room temperature and good

formabilities for achieving large contact areas with electrode active materials.

We previously reported that Na<sub>3</sub>PS<sub>4</sub> glass–ceramics in a metastable cubic phase obtained *via* a mechanochemical process and consecutive heat treatment exhibited a higher ionic conductivity than crystalline Na<sub>3</sub>PS<sub>4</sub> in the tetragonal phase.<sup>5</sup> The Na<sub>3</sub>PS<sub>4</sub> sulfide system possesses a better formability than the Li<sub>3</sub>PS<sub>4</sub> system, and its densification and associated sintering behavior are easily promoted by pressing at room temperature.<sup>6</sup> Subsequently, some sodium sulfides, such as Na<sub>3</sub>SbS<sub>4</sub> and Na<sub>11</sub>Sn<sub>2</sub>PS<sub>12</sub>, have been found to exhibit high ionic conductivities of over 1 mS cm<sup>−1</sup> at room temperature.<sup>7–11</sup> In particular, we reported a Na<sub>2.88</sub>Sb<sub>0.88</sub>W<sub>0.12</sub>S<sub>4</sub> glass–ceramic electrolyte with the highest ionic conductivity of 32 mS cm<sup>−1</sup> among sulfide lithium and sodium-ion conductors reported so far.<sup>12</sup>

Studies on solid electrolytes have thus far focused on sulfide systems with tetrahedral structure units, such as PS<sub>4</sub><sup>3−</sup> and SbS<sub>4</sub><sup>3−</sup>. In contrast, solid electrolytes composed of triangular structural units have not been extensively studied. Solid electrolytes containing B as a center element are known to have triangular boron units in the systems of Na<sub>2</sub>O–B<sub>2</sub>O<sub>3</sub> and Na<sub>2</sub>S–B<sub>2</sub>S<sub>3</sub>. We reported the preparation of Na<sub>3</sub>BO<sub>3</sub> orthoborate glass

<sup>a</sup> Department of Applied Chemistry, Graduate School of Engineering, Osaka Prefecture University, 1-1, Naka-ku, Sakai, Osaka 599-8531, Japan.

E-mail: hayashi@chem.osakafu-u.ac.jp

<sup>b</sup> Elements Strategy Initiative for Catalysts and Batteries Kyoto University, Kyoto University, Sakyo, Kyoto 606-8501, Japan

† Electronic supplementary information (ESI) available. See DOI: 10.1039/d0ma00777c

with a triangular  $\text{BO}_3^{3-}$  unit *via* a mechanochemical process, and its ionic conductivity was over  $10^{-8} \text{ S cm}^{-1}$ .<sup>13</sup> In general, the sodium-ion conductivity of glassy electrolytes increases with increasing Na content. The conductivities of  $\text{Na}_2\text{S-B}_2\text{S}_3$  glasses prepared by conventional melt quenching have only been investigated for compositions with less than 67 mol%  $\text{Na}_2\text{S}$ ,<sup>14</sup> while the conductivities of  $\text{Na}_3\text{BS}_3$  *ortho*-thioborate glasses with Na content higher than 75 mol%  $\text{Na}_2\text{S}$  have not been reported. Another challenge for developing the sodium thioborate system is the difficulty in obtaining pure  $\text{B}_2\text{S}_3$ , which is not commercially available. Although the synthesis of  $\text{B}_2\text{S}_3$  has been reported,<sup>15</sup> it is generally difficult to obtain pure  $\text{B}_2\text{S}_3$  due to its low chemical stability and tendency to easily oxidation.

In this study,  $\text{Na}_3\text{BS}_3$  sulfide electrolytes with three-coordinated borons were synthesized directly from a starting mixture of  $\text{Na}_2\text{S}$ , B, and S reagents. Crystalline  $\text{Na}_3\text{BS}_3$  (monoclinic phase) was prepared by a solid-phase reaction in advance, which was then used to prepare glassy  $\text{Na}_3\text{BS}_3$  *via* a mechanochemical process. A metastable crystalline phase was precipitated by crystallization of the prepared glassy  $\text{Na}_3\text{BS}_3$ . The structure and ionic conductivity of the prepared  $\text{Na}_3\text{BS}_3$  electrolytes were examined, and their application to all-solid-state sodium cells was investigated.

## 2. Experimental

A mixture of  $\text{Na}_2\text{S}$  (>99.1%; Nagao), crystalline B (>99%; Kojundo Chem.), and S (>99.99%; Kojundo Chem.) was pelletized and placed into a carbon crucible, then heated at 700 °C for 10 h in a quartz ampoule sealed under vacuum. After cooling to room temperature slowly, crystalline  $\text{Na}_3\text{BS}_3$  was obtained. The  $\text{Na}_3\text{BS}_3$  glass was prepared from the crystalline  $\text{Na}_3\text{BS}_3$  by a mechanochemical technique at an ambient temperature using a planetary ball mill (Pulverisette 7; Fritsch) with zirconia pots (45 mL in volume) and zirconia balls (4 mm in diameter, 45 g). The total mass of the starting materials was 0.4 g in each pot, and the rotational speed and milling duration were 310 rpm and 50 h, respectively. The milled sample powders were then heated in an electric furnace at 200 or 300 °C for 1 h. The heating temperatures were determined *via* differential thermal analysis (DTA). All processes were performed in a dry Ar atmosphere.

X-ray diffraction (XRD) measurements of the prepared materials were performed using  $\text{CuK}\alpha$  radiation with a diffractometer (SmartLab; Rigaku). The diffraction data were collected in steps of  $0.01^\circ$  in the  $2\theta$  range of  $10.0^\circ$ – $80.0^\circ$ . The XRD measurements were performed using an airtight vessel with a beryllium window to prevent exposure of the sample to the air. The crystalline structures were refined using the SLS2 software (Rigaku), and the heated sample patterns were refined using the Rietveld method in the software package RIETAN-FP.<sup>16</sup>

<sup>11</sup>B solid-state NMR experiments were performed using an NMR spectrometer (JNM-ECX 400; JEOL). The sample powders

were packed into zirconia spinners in a dry Ar atmosphere. The observation frequency was 128.3 MHz. The spectra were acquired using a single pulse with a pulse width of 1.17  $\mu\text{s}$  (1/3 of  $90^\circ$  pulse width), a recycle pulse delay of 0.5 s, and an MAS rate of 12 kHz. The chemical shifts were calibrated using  $\text{BPO}_4$  (−3.6 ppm).

Raman spectra of the samples were measured using a Raman spectrophotometer (LabRAM HR-800; Horiba) with a 532 nm solid-state laser to identify the structural units. The electrolyte samples were placed in an airtight vessel with a quartz window. The process was performed in a dry Ar atmosphere.

DTA was performed using a thermal analyzer (Thermo Plus TG8110; Rigaku) at a heating rate of  $10^\circ\text{C min}^{-1}$  under  $\text{N}_2$  gas. The milled samples were sealed in Al pans in a dry Ar atmosphere.

The ionic conductivities were determined *via* AC impedance measurements using an impedance analyzer (Solartron; 1260) in the frequency range from 10 Hz to 1 MHz with an applied AC voltage of 50 mV. The measurements were carried out using compressed powder pellets (diameter of 10 mm and thickness of 1 mm). Gold thin films (diameter of 10 mm) as ion-blocking electrodes were deposited on both faces of the pellets with a quick coater (Quick coater SC-701; Sanyu Electron). Each pellet was sealed in a laminate-type pouch cell to prevent air exposure.

The electronic conductivity was measured using the DC polarization technique. The sample powders were pressed at 360 MPa, and gold current collectors were used to cover the surfaces of the pellets. Each pellet was sealed in a laminate-type pouch cell. The data were collected using a potentio/galvanostat (1287, Solartron) with the applied DC voltage of 0.16 V at room temperature.

The densities of the powder-compressed pellets ( $d_1$ ) were calculated from the weight and volume of the pellets, and those of the powders ( $d_2$ ) were measured using a gas pycnometer (AccuPyc II 1340; Shimadzu). The relative density was defined as  $d_1/d_2$ . The microstructures of the cross-sections of the pellets were observed *via* scanning electron microscopy (SEM) (JSM-6610A; JEOL).

Cyclic voltammetry was conducted to investigate the electrochemical properties of the prepared  $\text{Na}_3\text{BS}_3$  glass electrolyte. A composite electrode (80 mg) with  $\text{Na}_{15}\text{Sn}_4$  (80 wt%) and Ketjen Black (KB, 20 wt%) was used as a counter electrode,<sup>17</sup> and a stainless-steel rod was used as a working electrode. The potential sweep was performed between −0.5 V and 5.0 V with a scanning rate of  $5.0 \text{ mV min}^{-1}$  at 60 °C.

All-solid-state cells were constructed as follows. The  $\text{Na}_3\text{BS}_3$  glass powder (80 mg) was used as the solid electrolyte. A composite (2.7 mg) of  $\text{TiS}_2$  (99%; Kojundo Chem., 40 wt%) and the electrolyte (60 wt%) was used as the positive electrode, and the composite of  $\text{Na}_{15}\text{Sn}_4$ –KB (30 mg) was used as the negative electrode. The prepared all-solid-state cells were charged and discharged at 60 °C in the voltage range from 1.2 to 2.4 V at  $0.038 \text{ mA cm}^{-2}$  under an Ar atmosphere. CV and charge–discharge measurement for the all-solid-state cells were using a potentio/galvanostat device (Bio-logic, VMP-3).



### 3. Results

Fig. 1 shows the XRD patterns of the  $\text{Na}_3\text{BS}_3$  crystalline, glassy, and glass-ceramic samples. The XRD pattern of crystalline  $\text{Na}_3\text{BS}_3$  was the same as that reported for  $\text{Na}_3\text{BS}_3$  (ICSD: 411608, monoclinic structure<sup>18</sup>). From  $\text{Na}_2\text{S}$ , B, and S as starting materials, crystalline  $\text{Na}_3\text{BS}_3$  was successfully synthesized by a conventional solid-phase reaction. The crystal was then mechanochemically treated, and the obtained sample showed a halo XRD pattern and an endothermic change attributable to the glass transition at 175 °C ( $T_g$ ) on the DTA curve, as shown in Fig. 2. The glassy  $\text{Na}_3\text{BS}_3$  electrolyte was then obtained by a two-step process: synthesis of crystalline  $\text{Na}_3\text{BS}_3$  from  $\text{Na}_2\text{S}$ , B, and S and amorphization of the crystal. By using this two-step process, the glass-forming region of sodium thioborates was determined. As shown in Fig. S1 (ESI<sup>†</sup>), the XRD pattern attributable to  $\text{Na}_2\text{S}$  as a starting reagent was observed at compositions of  $x = 0.76$  and higher for the  $x\text{Na}_2\text{S} \cdot (1-x)\text{B}_2\text{S}_3$  samples. Glassy electrolytes were prepared in the range of  $0.33 \leq x \leq 0.75$  in this study. The glass composition with the highest Na content,  $x = 0.75$ , corresponds to the *ortho*-thioborate  $\text{Na}_3\text{BS}_3$ .

The  $\text{Na}_3\text{BS}_3$  glass was heated at 200 or 300 °C corresponding to the exothermic peaks in the DTA curve, as shown in Fig. 2. After heating at 200 °C, a new metastable phase was observed. The XRD pattern was similar to that of the reported monoclinic  $\text{Na}_3\text{BS}_3$  phase, which is thermodynamically stable, but the new phase was indexed to a higher symmetry. The detailed structural analysis is discussed later. After heating at 300 °C, the



Fig. 2 DTA curve of  $\text{Na}_3\text{BS}_3$  glass. The orange arrow shows the glass transition temperature, and the two black arrows show the heat-treatment temperatures employed to prepare the glass-ceramics.

glass-ceramic showed almost the same XRD pattern as that of the monoclinic  $\text{Na}_3\text{BS}_3$  phase.

The local structure of the  $\text{Na}_3\text{BS}_3$  samples was analyzed by  $^{11}\text{B}$  MAS-NMR measurements and Raman spectroscopy. Fig. 3 shows the  $^{11}\text{B}$  MAS-NMR spectra of the  $\text{Na}_3\text{BS}_3$  solid electrolytes, where the peaks marked with asterisks are spinning side bands. All the samples showed similar spectra. The two resonance peaks between 50 and 70 ppm are attributable to triangular  $\text{BS}_3$  units with three-coordinated boron, and the highly symmetrical peaks at 0 and 10 ppm are attributable to tetrahedral  $\text{BO}_x\text{S}_{4-x}$  units with four-coordinated boron.<sup>14</sup> The peaks corresponding to the tetrahedral units were hardly

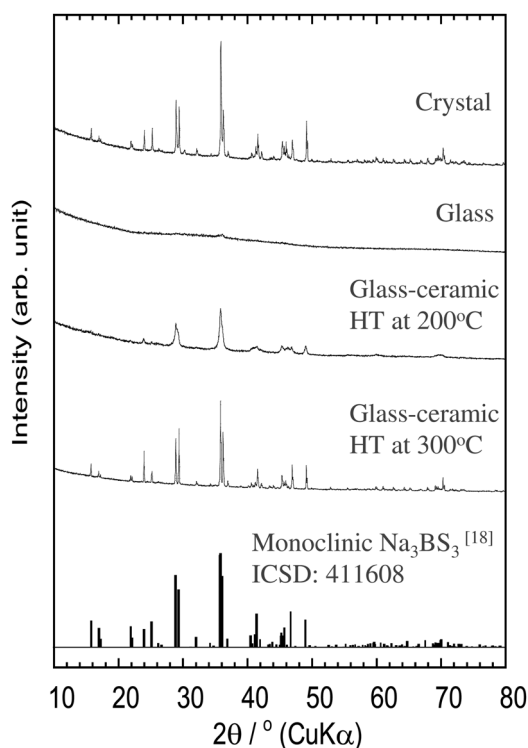


Fig. 1 XRD patterns of  $\text{Na}_3\text{BS}_3$  solid electrolytes.



Fig. 3  $^{11}\text{B}$  MAS-NMR spectra of  $\text{Na}_3\text{BS}_3$  solid electrolytes.



Fig. 4 Raman spectra of  $\text{Na}_3\text{BS}_3$  solid electrolytes.

observed for the  $\text{Na}_3\text{BS}_3$  glass, suggesting that the glass mainly consisted of triangular  $\text{BS}_3$  units.

The Raman spectra of the  $\text{Na}_3\text{BS}_3$  samples are shown in Fig. 4. The crystal and glass-ceramics showed similar spectra with a sharp band at  $435\text{ cm}^{-1}$  and broad bands at  $470$ ,  $765$ , and  $940\text{ cm}^{-1}$ , all of which are attributable to triangular  $\text{BS}_3$  units.<sup>19</sup> The residual broad band at  $795\text{ cm}^{-1}$  is expected to be attributable to tetrahedral  $\text{BO}_x\text{S}_{4-x}$  units since they were detected by  $^{11}\text{B}$  MAS-NMR. The spectrum of  $\text{Na}_3\text{BS}_3$  glass was broader than that of the  $\text{Na}_3\text{BS}_3$  crystal because of its amorphous nature. Thus, it was concluded that the local structures of all the  $\text{Na}_3\text{BS}_3$  samples were similar.

Fig. 5(a) shows the Rietveld refinement profile for the  $\text{Na}_3\text{BS}_3$  glass-ceramic heated at  $200^\circ\text{C}$ . Structural optimization of the new metastable phase resulted in a trigonal crystal structure. The observed and calculated XRD patterns (red and black lines, respectively) were in good agreement, as indicated by their difference spectrum (blue line). Table 1 summarizes the crystallographic parameters including the lattice constants, positions of atoms, thermal factors, and atomic occupancies of the  $\text{Na}_3\text{BS}_3$  glass-ceramic obtained from the Rietveld refinement. The lattice parameters were  $a = 3.90\text{ \AA}$ ,  $c = 7.42\text{ \AA}$ ,  $\alpha = \beta = 90^\circ$ , and  $\gamma = 120^\circ$ , and the space group was  $P3$  (No. 143). The trigonal phase had a higher symmetry than the monoclinic phase of crystalline  $\text{Na}_3\text{BS}_3$ , as shown in Table S1 (ESI†).

Fig. 5(b) and Fig. S2(a) (ESI†) show schematic diagrams of trigonal and monoclinic  $\text{Na}_3\text{BS}_3$ ,<sup>18</sup> respectively, generated by the VESTA visualization program. The red, green, and yellow spheres are Na, B, and S, respectively. The major difference between the metastable and stable structures is the distortion of the six-membered ring consisting of B and S atoms. For ease of understanding, Fig. S2(b) (ESI†) shows an image diagram of the monoclinic structure; the Na layers and B-S layers located

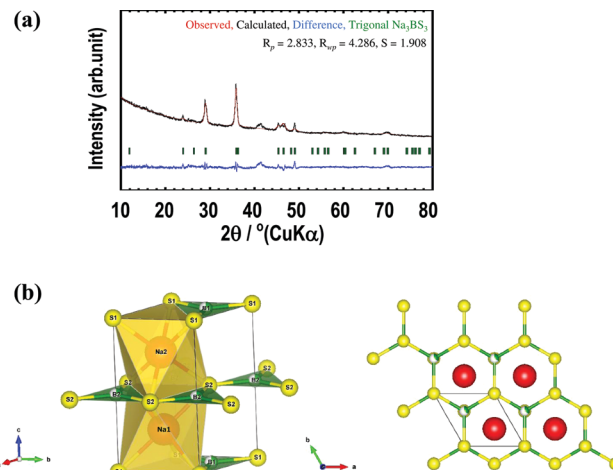


Fig. 5 Crystal structure analysis of  $\text{Na}_3\text{BS}_3$  metastable phase. (a) X-ray Rietveld refinement profile for the  $\text{Na}_3\text{BS}_3$  glass-ceramic heated at  $200^\circ\text{C}$ . Solid red and black lines denote the observed and calculated XRD patterns, respectively, and the difference between the curves is shown in blue. The green ticks mark the positions of the reflection allowed by the space group of trigonal  $\text{Na}_3\text{BS}_3$ . (b) Schematic diagram of the crystal structure of trigonal  $\text{Na}_3\text{BS}_3$ . Red, green, and yellow spheres are Na, B, and S, respectively.

at different  $z$ -positions are shown on the left. Na sites were added to a selected B-S layer. One-third of the B sites of the B-S layers are occupied, and the vacancy sites are shown as gray spheres. In the trigonal structure, the six-membered rings are not distorted because B atoms randomly occupy **1a** or **1b** sites. Conversely, in the monoclinic structure, the B atoms are located at only one of the three sites of the six-membered rings, leading to a distorted framework.

The temperature dependence of the ionic conductivities of the  $\text{Na}_3\text{BS}_3$  samples is shown in Fig. 6(a), and the Nyquist plot of  $\text{Na}_3\text{BS}_3$  glass at room temperature is shown in Fig. S3 (ESI†). A semicircle in the higher-frequency region and spike in the lower-frequency region were observed in the Nyquist plot. The insert figure in the Fig. S3 (ESI†) is an equivalent circuit consisting of resistance and constant phase element (CPE). The  $\text{CPE}_2$  of the equivalent circuit reflects the capacitance from the Au current collector. The bulk and grain-boundary contributions were not reliably separated and thus the herein reported conductivities were calculated from total resistance  $R$ . The glass-ceramic heated at  $300^\circ\text{C}$  had a low ionic conductivity, and thus it was measured only at  $106^\circ\text{C}$ . For the other samples, the temperature dependence of the ionic conductivities obeyed the Arrhenius equation, and thus the activation energies were calculated from the Arrhenius plots. Their ionic conductivities at  $25^\circ\text{C}$  (calculated from the Arrhenius equation) and activation energies are summarized in Table 2; for the glass-ceramic heated at  $300^\circ\text{C}$ , the experimental conductivity determined at  $106^\circ\text{C}$  is listed. The room-temperature ionic conductivity and activation energy of the  $\text{Na}_3\text{BS}_3$  glass were  $1.1 \times 10^{-5}\text{ S cm}^{-1}$  and  $39\text{ kJ mol}^{-1}$ , respectively. This conductivity is higher than those of  $\text{Na}_3\text{BO}_3$  glass<sup>13</sup> and  $\text{Na}_3\text{PS}_4$  glass,<sup>5</sup> as shown in Fig. 6(b). The ionic conductivities at





**Table 1** Atomic coordinates of the Na<sub>3</sub>BS<sub>3</sub> metastable phase

Phase			Na <sub>3</sub> BS <sub>3</sub>			
Crystal system			Trigonal			
Space group			<i>P</i> 3 (No. 143)			
Lattice parameter, volume, <i>Z</i>			<i>a</i> = 3.901(1) Å, <i>c</i> = 7.422(1) Å, <i>V</i> = 97.83(1) Å <sup>3</sup> <i>α</i> = 90, <i>β</i> = 90, <i>γ</i> = 120, <i>Z</i> = 1			
Atoms	<i>x</i>	<i>y</i>	<i>z</i>	Site	Occupancy	<i>B</i>
Na1	0.6667	0.3333	0.2467(1)	1c	1.0000	1.000
Na2	0.6667	0.3333	0.7468(1)	1c	1.0000	1.000
S1	0.0000	0.0000	0.0000	1a	1.0000	1.000
S2	0.3333	0.6667	0.5000	1b	1.0000	1.000
B1	0.3333	0.6667	0.0000	1b	0.3333	1.000
B2	0.0000	0.0000	0.5000	1a	0.3333	1.000

**Fig. 6** Temperature dependence of conductivity for (a) Na<sub>3</sub>BS<sub>3</sub> glass, glass-ceramics, and crystal electrolytes and (b) Na<sub>3</sub>BS<sub>3</sub>, Na<sub>3</sub>PS<sub>4</sub>,<sup>5</sup> and Na<sub>3</sub>BO<sub>3</sub>,<sup>13</sup> glass electrolytes.**Table 2** Ionic conductivities at room temperature ( $\sigma_{25}$ ), activation energies ( $E_a$ ), densities of pellets ( $d_1$ ) and powders ( $d_2$ ), and relative density ( $d_1/d_2$ ) of Na<sub>3</sub>BS<sub>3</sub> solid electrolytes

	$\sigma_{25}/\text{S cm}^{-1}$	$E_a/\text{kJ mol}^{-1}$	$d_1$ (g cm <sup>-3</sup> )	$d_2$ (g cm <sup>-3</sup> )	Relative density (%)
Crystal	$3.7 \times 10^{-10}$	79	1.725	1.996	86.4
Glass	$1.1 \times 10^{-5}$	39	1.824	1.932	94.4
g.c. (HT200 °C)	$1.2 \times 10^{-8}$	55	1.529	1.999	76.5
g.c. (HT300 °C)	$8.0 \times 10^{-8}$ (at 106 °C)	—	1.701	2.001	85.0

$d_1$ : density calculated from the volume measured by dimension of the pellet.  $d_2$ : density calculated from the volume measured by a gas pycnometer.

25 °C and activation energies of other reported sodium-ion conducting glassy electrolytes are summarized in Table S2 (ESI†).<sup>5,13,14,20,21</sup> The electronic conductivity at room temperature measured *via* DC polarization was  $7.6 \times 10^{-10} \text{ S cm}^{-1}$ , which is five orders of magnitude lower than the ionic conductivity. Thus, the sodium-ion transport number of the Na<sub>3</sub>BS<sub>3</sub> glass was almost unity. Fig. S4 (ESI†) shows the room-temperature ionic conductivities and activation energies of the  $x\text{Na}_2\text{S} \cdot (1-x)\text{B}_2\text{S}_3$  ( $0.33 \leq x \leq 0.75$ ) glass electrolytes. In the glass-forming region, Na<sub>3</sub>BS<sub>3</sub> glass showed the highest ionic conductivity and the lowest activation energy because of its highest Na content.

The glass showed the highest ionic conductivity among the prepared Na<sub>3</sub>BS<sub>3</sub> solid electrolytes. Between the glass-ceramics heated at 200 and 300 °C, the former showed a higher ionic conductivity. Table 2 lists the densities of the powder-compressed pellets ( $d_1$ ) and powders ( $d_2$ ) and the relative densities ( $d_1/d_2$ ) of the Na<sub>3</sub>BS<sub>3</sub> solid electrolytes. After heat treatment, the glass-ceramics showed lower relative densities than the glass because of crystal precipitation. The Na<sub>3</sub>BS<sub>3</sub> glass pressed at 360 MPa showed the highest relative density of 94%, which is higher than that of Na<sub>3</sub>BO<sub>3</sub> glass (88%) pressed at 720 MPa.<sup>13</sup> This is related to the fact that the sulfide ion has a larger polarizability than the oxide ion. The high relative density means that the Na<sub>3</sub>BS<sub>3</sub> glass has a favorable formability. Of other sulfide-based solid electrolytes, the relative density of Na<sub>3</sub>PS<sub>4</sub> glass pressed at 360 MPa was 94%,<sup>6</sup> indicating that the Na<sub>3</sub>BS<sub>3</sub> glass has a similar formability. Fig. 7 shows an SEM image of the fractured cross-section of the powder-compressed pellet of the Na<sub>3</sub>BS<sub>3</sub> glass, indicating that the glass showed good formability.

Cyclic voltammetry was conducted to investigate the electrochemical properties of the Na<sub>3</sub>BS<sub>3</sub> glass. Fig. S5(a) (ESI†) shows cyclic voltammogram of an all-solid-state two-electrode cell using the Na<sub>3</sub>BS<sub>3</sub> glass electrolyte. Stainless-steel and Na<sub>15</sub>Sn<sub>4</sub>-KB were used as working and counter electrodes, respectively. The potential sweep was performed with a scanning rate of 5.0 mV min<sup>-1</sup> at 60 °C. Reduction and oxidation currents attributable to sodium deposition and dissolution

**Fig. 7** Cross-sectional SEM image of the Na<sub>3</sub>BS<sub>3</sub> glass.



Fig. 8 Charge-discharge curves of the all-solid-state cell  $\text{Na}_{15}\text{Sn}_4/\text{Na}_3\text{BS}_3$  glass/ $\text{TiS}_2$  cell at 60 °C and a current density of 0.038  $\text{mA cm}^{-2}$  in the potential range of 1.2–2.4 V.

were observed at around 0 V *versus* the counter electrode, and no remarkable oxidation current was observed up to 5.0 V. This suggests that the  $\text{Na}_3\text{BS}_3$  glass has a wide electrochemical window of 5.0 V. Fig. S5(b) (ESI<sup>†</sup>) shows the cross-sectional SEM image of the cell after cyclic voltammetry. The working electrode of stainless steel was removed from the cell and two layers of  $\text{Na}_3\text{BS}_3/\text{Na}_{15}\text{Sn}_4\text{-KB}$  were observed. A close contact at the interface between the two layers was maintained and unfavourable deterioration for the interface was not observed.

The  $\text{Na}_3\text{BS}_3$  glass was used as an electrolyte in an all-solid-state cell. Fig. 8 shows the initial five charge-discharge curves of the all-solid-state  $\text{Na}_{15}\text{Sn}_4/\text{Na}_3\text{BS}_3$  glass/ $\text{TiS}_2$  cell. The cell was operated as a sodium secondary battery at 60 °C, where the conductivity of the  $\text{Na}_3\text{BS}_3$  glass was  $5.8 \times 10^{-5} \text{ S cm}^{-1}$ , and showed an initial charge capacity of 190  $\text{mA h g}^{-1}$ . A capacity of approximately 170  $\text{mA h g}^{-1}$  was retained from the second to the fifth cycle, suggesting that  $\text{Na}_3\text{BS}_3$  glass is adopted as a solid electrolyte for all-solid-state cells manufactured only by pressing.

## 4. Discussion

Compared with the ionic conductivities of the glass-ceramics, the glass-ceramic heated at 200 °C showed higher ionic conductivity than that heated at 300 °C. This was due to the obtaining of the metastable phase with a higher ionic conductivity than the stable phase. The activation energy of metastable phase was 55  $\text{kJ mol}^{-1}$ . That of stable phase of glass-ceramic was not measured, but the activation energy of the  $\text{Na}_3\text{BS}_3$  crystal which showed the same stable phase was 79  $\text{kJ mol}^{-1}$ . It suggests that the activation barrier to ion conduction of metastable phase was smaller than that of stable phase due to the higher symmetry of the structure.

The ionic conductivity of the glass was higher than those of the glass-ceramics and crystal because of the random structure and free volume for ionic conduction. Moreover, this

conductivity is higher than that of  $\text{Na}_3\text{PS}_4$  glass.<sup>5</sup> These relative densities were same value (94%).<sup>6</sup> Thus, the difference between these ionic conductivities is not caused by their formabilities. The activation energy of  $\text{Na}_3\text{BS}_3$  glass was 39  $\text{kJ mol}^{-1}$ , which was lower than that of  $\text{Na}_3\text{PS}_4$  glass (47  $\text{kJ mol}^{-1}$ ).<sup>5</sup> This suggests that the activation barrier to ion conduction of the  $\text{Na}_3\text{BS}_3$  glass with planar triangular  $\text{BS}_3$  units is smaller than that of the  $\text{Na}_3\text{PS}_4$  glass with tetrahedral  $\text{PS}_4$  units. It was also found that the mean atomic volumes of the  $\text{Na}_3\text{BS}_3$  glass and  $\text{Na}_3\text{PS}_4$  glass were calculated using the powder densities of these glasses (1.932  $\text{g cm}^{-3}$  of  $\text{Na}_3\text{BS}_3$  glass and 2.002  $\text{g cm}^{-3}$  of  $\text{Na}_3\text{PS}_4$  glass). The mean atomic volume of the  $\text{Na}_3\text{BS}_3$  glass is 13.0  $\text{cm}^3 \text{ mol}^{-1}$ , which is smaller than that of the  $\text{Na}_3\text{PS}_4$  glass (14.2  $\text{cm}^3 \text{ mol}^{-1}$ ). It suggests the high ionic conductivity of  $\text{Na}_3\text{BS}_3$  glass is related with its larger packing density compared to the  $\text{Na}_3\text{PS}_4$  glass.

## 5. Conclusions

The  $\text{Na}_3\text{BS}_3$  glassy electrolyte was prepared and its electrical and electrochemical properties were examined for the first time. The new metastable  $\text{Na}_3\text{BS}_3$  phase with a trigonal structure was formed as a primary phase by crystallization of the  $\text{Na}_3\text{BS}_3$  glass, and showed a higher ionic conductivity than the previously reported monoclinic  $\text{Na}_3\text{BS}_3$  phase. The room-temperature ionic conductivity and activation energy of the  $\text{Na}_3\text{BS}_3$  glass were  $1.1 \times 10^{-5} \text{ S cm}^{-1}$  and 39  $\text{kJ mol}^{-1}$ , respectively and its crystallization decreased conductivity. In addition, the  $\text{Na}_3\text{BS}_3$  glass showed a favorable formability. The all-solid-state cell operated with the prepared glass as the electrolyte exhibited a reversible capacity of approximately 170  $\text{mA h g}^{-1}$  during five charge-discharge cycles at 60 °C. It is concluded that the  $\text{Na}_3\text{BS}_3$  glass with triangular structural units has appropriate properties as a solid electrolyte for application to all-solid-state sodium batteries. The results of this study extend research toward designing multi-component sulfide electrolytes with triangular  $\text{BS}_3$  structural units and contribute to the development of solid electrolytes for all-solid-state batteries.

## Conflicts of interest

There are no conflicts to declare.

## Acknowledgements

This work was supported by the Element Strategy Initiative of MEXT, Grant Number JPMXP0112101003, and JSPS KAKENHI Grant Numbers 18H01713 and 19H05816.

## References

- 1 B. L. Ellis and L. F. Nazar, *Curr. Opin. Solid State Mater. Sci.*, 2012, **16**, 168.
- 2 K. B. Hueso, M. Armand and T. Rojo, *Energy Environ. Sci.*, 2013, **6**, 734.



- 3 H. Pan, Y.-S. Hu and L. Chen, *Energy Environ. Sci.*, 2013, **6**, 2338.
- 4 X. Lu, G. Xia, J. P. Lemmon and Z. Yang, *J. Power Sources*, 2010, **195**, 2431.
- 5 A. Hayashi, K. Noi, A. Sakuda and M. Tatsumisago, *Nat. Commun.*, 2012, **3**, 856.
- 6 M. Nose, A. Kato, A. Sakuda, A. Hayashi and M. Tatsumisago, *J. Mater. Chem. A*, 2015, **3**, 22061.
- 7 A. Banerjee, K. H. Park, J. W. Heo, Y. J. Nam, C. K. Moon, S. M. Oh, S. T. Hong and Y. S. Jung, *Angew. Chem., Int. Ed.*, 2016, **55**, 9634.
- 8 H. Wang, Y. Chen, Z. D. Hood, G. Sahu, A. S. Pandian, J. K. Keum, K. An and C. Liang, *Angew. Chem., Int. Ed.*, 2016, **55**, 8551.
- 9 L. Zhang, D. Zhang, K. Yang, X. Yan, L. Wang, L. Mi, B. Xu and Y. Li, *Adv. Sci.*, 2016, **3**, 1600089.
- 10 M. Duchardt, U. Ruschewitz, S. Adams, S. Dehnen and B. Roling, *Angew. Chem., Int. Ed.*, 2018, **57**, 1351.
- 11 Z. Zhang, E. Ramos, F. Lalère, A. Assoud, K. Kaup, P. Hartman and L. F. Nazar, *Energy Environ. Sci.*, 2018, **11**, 87.
- 12 A. Hayashi, N. Masuzawa, S. Yubuchi, F. Tsuji, C. Hotehama, A. Sakuda and M. Tatsumisago, *Nat. Commun.*, 2019, **10**, 5266.
- 13 K. Suzuki, Y. Nakamura, N. Tanibata, A. Hayashi and M. Tatsumisago, *J. Asian Ceram. Soc.*, 2016, **4**, 6.
- 14 D. Larink, H. Eckert and S. W. Martin, *J. Phys. Chem. C*, 2012, **116**, 22698.
- 15 S. W. Martin and D. R. Bloyer, *J. Am. Ceram. Soc.*, 1990, **73**, 3481.
- 16 F. Izumi and K. Momma, *Solid State Phenom.*, 2007, **130**, 15.
- 17 A. Hayashi, K. Noi, N. Tanibata, M. Nagao and M. Tatsumisago, *J. Power Sources*, 2014, **258**, 420.
- 18 J. Kuchinke, C. Jansen, A. Lindemann and B. Krebs, *Z. Anorg. Allg. Chem.*, 2001, **627**, 896.
- 19 M. Royle, J. Cho and S. W. Martin, *J. Non-Cryst. Solids*, 2001, **279**, 97.
- 20 I. A. Sokolov, V. N. Naraev and A. A. Pronkin, *Glass Phys. Chem.*, 2000, **26**, 588.
- 21 M. Nose, A. Kato, A. Sakuda, A. Hayashi and M. Tatsumisago, *J. Mater. Chem. A*, 2015, **44**, 22061.

